

## **Chapter 4**

# **Effects of the loss of symmetry on the wall shear stresses in Abdominal Aortic Aneurysms**

### **A. Introduction**

Owing to their effect on the endothelial cells, wall shear stresses appear to be one of the most physiologically relevant parameter to characterize in order to improve the current understanding of the pathological processes accounting for the growth of AAAs. The evolution of the wall shear stresses during the aneurismal growth in symmetric models have been discussed in Chapter 3. This chapter is devoted to the analysis of the effects of the loss of symmetry on the flow structures and patterns of wall shear stresses. Medium to large size aneurysms (diameter  $> 4$  cm) tend to be non-symmetric due to the presence of the vertebral column, which brings some structural support and prevent the growth in the posterior direction. It can be noticed, as detailed in the general introduction, that very few studies have involved non-symmetric models of aneurysm. None of the studies considered the changes in the wall shear stresses inside the AAA. Thus, the objective of this chapter is to quantify the changes in the spatial and temporal distribution of WSS in AAAs at progressive stages of asymmetry.

Precise measurements of the velocity field have been conducted using Particle Image Velocimetry (PIV). The evolution of the hemodynamics and WSS patterns are shown in section C. The physiological consequences of the measured patterns of WSS on the endothelial cells are detailed in section D.

## **B. Experimental setup**

In order to study the effects of the loss of axisymmetry on the flow characteristics in AAAs, three aneurysm models have been considered, one symmetric (model 16) and 2 non-symmetric (models 17 and 18) (see Table 2.I). The three models have the same dilatation ratio ( $D/d = 2.3$ ) and aspect ratio ( $L/d = 4.5$ ), but an increasing asymmetry parameter ( $\beta = 0, 0.5$  and  $1$  respectively).

PIV measurements of the instantaneous velocity field were conducted inside the two perpendicular planes (planes BB and CC) indicated in Figure 2.3 using the method described in Chapter 2.

## **C. Results**

### **1. Flow characteristics in abdominal aortic aneurysms**

#### **Flow field in a symmetric AAA**

Most fusiform aneurysms with a maximum diameter greater than 4 cm grow non-symmetrically. It is therefore important to understand how the flow properties change when the asymmetry parameter is increased. We shall first describe the flow in the symmetric model (model 16), which will serve as the reference case in this part of the study. The effects of the loss of symmetry will be discussed in the next sub-section. A detailed description of the evolution of the flow field in symmetric aneurysms at different stages of enlargement has already been reported in the previous chapter. For the purpose

of comparison, we discuss here the flow field in the symmetric model that has the same dilatation and aspect ratios as the non-symmetric models ( $D/d = 2.3$ ,  $L/d = 4.5$ ), which has not been discussed in Chapter 3. Thus, this chapter concentrates on the sole effect of increasing the asymmetric parameter. A new reference case is therefore defined in this chapter.

The velocity field has been measured in a central axial plane of the aneurysm using the PIV system with a mesh size of  $0.06d \times 0.06d$ . Figure 4.1 shows the instantaneous velocity field in the symmetric model (model 16) and Figure 4.2 the corresponding vorticity and stress fields at times B through E (see Appendix B for the stress calculation). The same fields are shown in Figure 4.3 phase-averaged over 6 cardiac cycles. Note that the total stress, non-dimensionalized by the peak value measured in the healthy aorta, ranges from 0 to 1, when the non-dimensionalized vorticity ranges from  $-1$  to 1. The red scale corresponds to positive values and the blue scale to negative ones. A hyperbolic tangent color scale was chosen in order to better visualize the inner flow features, a linear scale showing only the flow dynamics at the walls.

During the accelerating phase of the systole, the flow remains attached to the walls despite the large dilatation ratio of the model (Figure 4.1 B). This is a consequence of the positive pressure gradient that dominates at the beginning of systole, as the temporal flow acceleration is larger than the convective deceleration due to the increase in the diameter inside the aneurysm. Although the flow meanders slightly, it remains laminar with the bulk of the flow almost inviscid and irrotational (Figure 4.2 B). The vorticity and shear stress are concentrated along the walls and confined to thin Stokes layers.

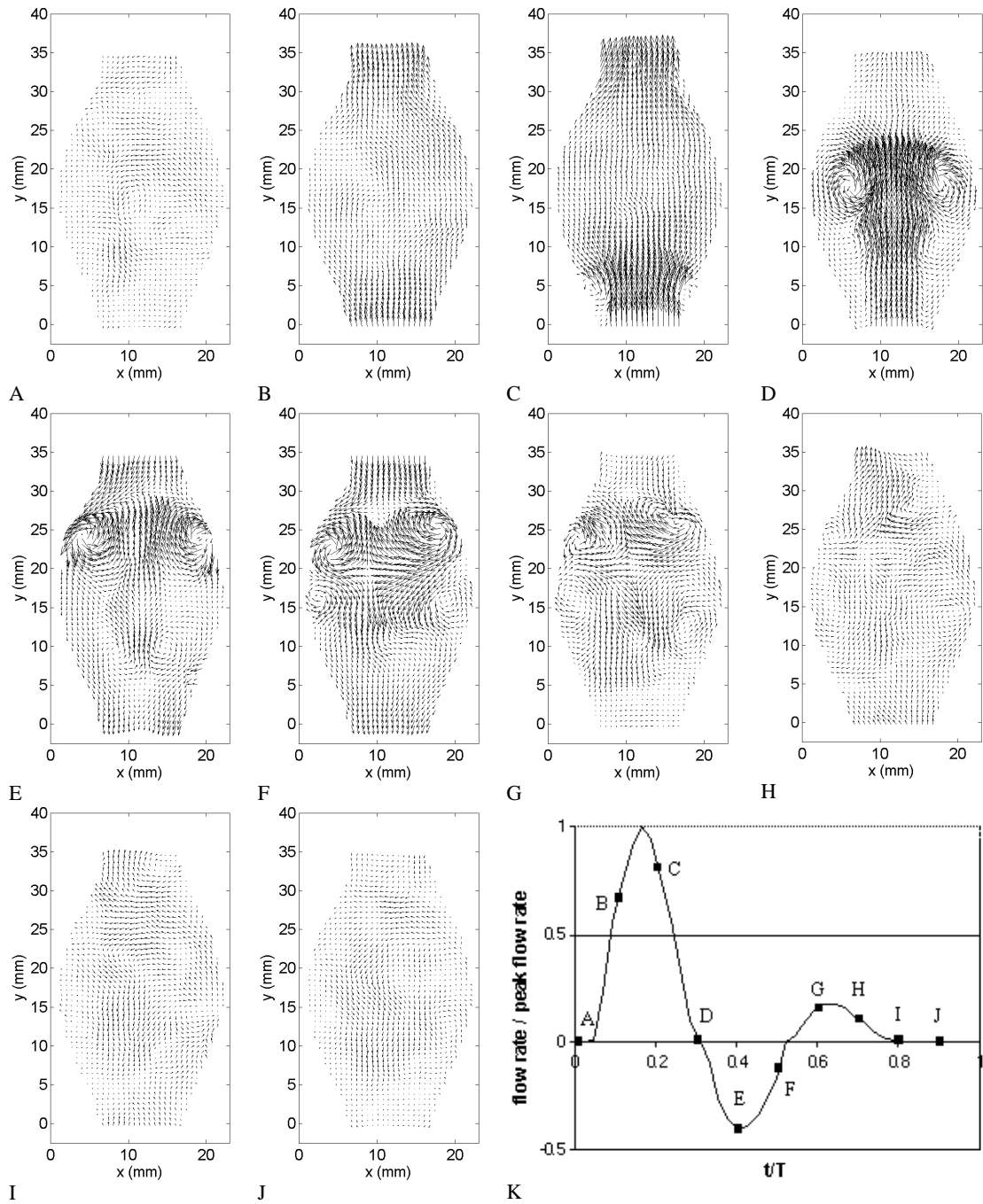


Figure 4.1: Instantaneous velocity field measured in the symmetric model (model 16) with the PIV system during one cardiac cycle.

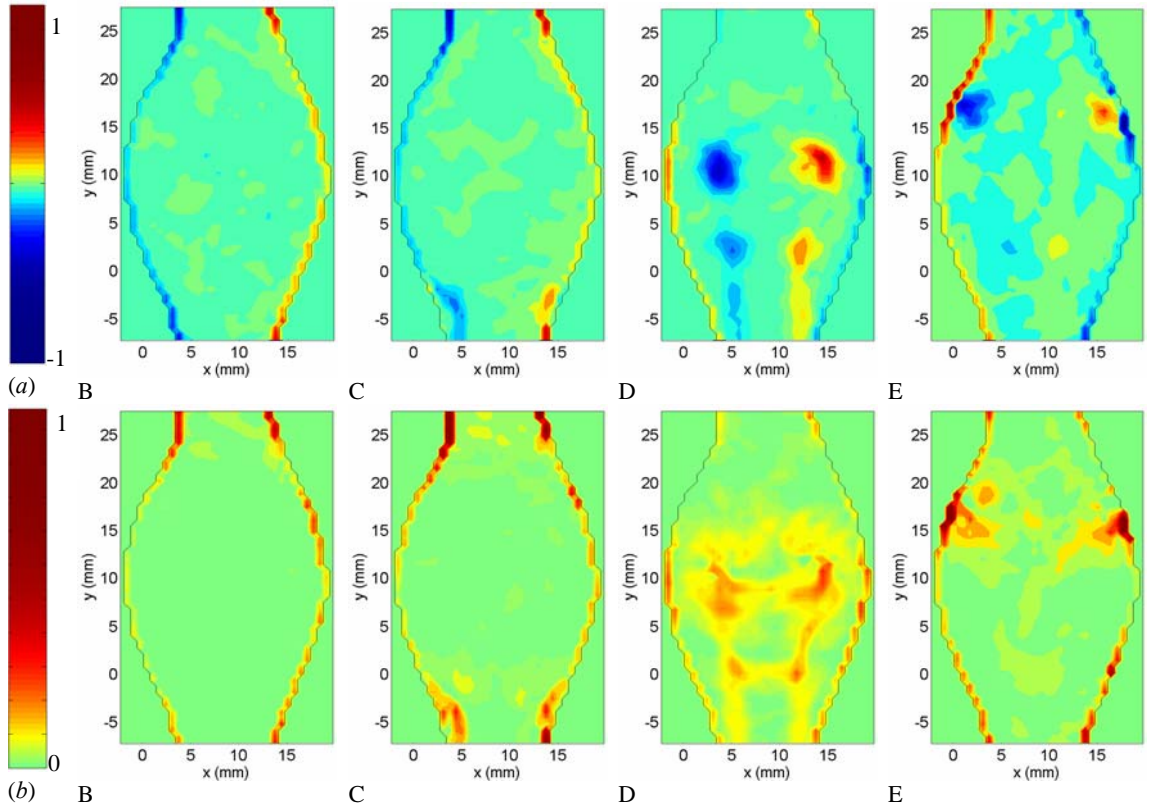


Figure 4.2: Instantaneous vorticity (a) and stress (b) fields measured in the symmetric model with the PIV system and non-dimensionalized by the peak systolic value measured in the healthy vessel.

One of the main characteristics of aneurysmal flow is its detachment from the proximal (entrance) wall in the decelerating phase of the systole (Figure 4.1 C). A strong start-up vortex ring forms proximally, while the flow remains attached to the wall downstream of it. The primary vortex ring travels along the aneurysm cavity and, as a result of the Kelvin Helmholtz instability, secondary vortices develop in the internal shear layer that is generated behind the start-up vortex (Figures 4.1 and 4.3 (a) D). These vortex rings can also be clearly seen in the vorticity plots (Figures 4.2 and 4.3 (b-c) D). The detachment of the flow from the wall leads to the formation of a large recirculating flow region that surrounds the core of the flow that is still moving forward. This region that extends over the first half of the aneurysm, is dominated by very low velocities and very small wall shear stresses as will be discussed in the next section.

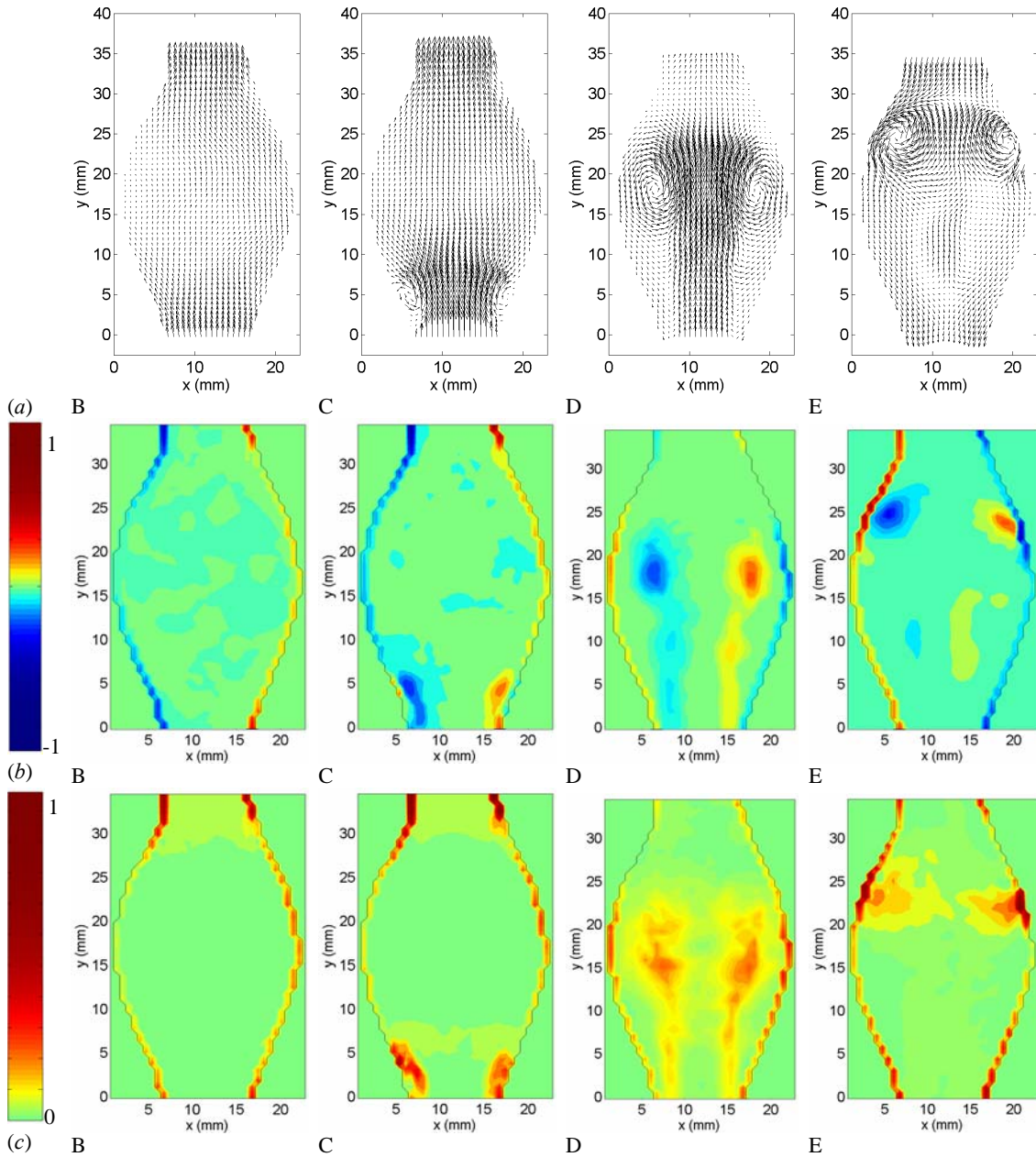


Figure 4.3: Non-dimensionalized phase-averaged velocity (a), vorticity (b) and stress (c) fields measured in the symmetric model with the PIV system.

In the symmetric model, the ratio  $l/d$ , where  $l$  is the maximum distance available to the vortex ring to travel inside the aneurysm, is equal to 2.5 and is therefore less than the systolic Strouhal number ( $St_{syst} = 3$ ), which is the controlling parameter of the vortex shedding (Chapter 3). This explains why the vortex ring impinges on the distal neck of

the aneurysm, generating very high negative shear stresses at the point of impact (time E in Figures 4.1, 4.2 and 4.3).

It should be noted that even in this symmetric geometry, a loss in the symmetry of the flow occurs as the primary vortex ring impinges on the distal wall (Figure 4.1 E). The flow becomes even more disorganized at time F, when the Stokes layers roll up into a counter-rotating vortex ring upstream of the primary ring (Figure 4.1 F). The intensity of these weakly turbulent motions decreases in the resting portion of the cardiac cycle due to viscous dissipation (Figure 4.1 G-J). The flow almost returns to a stagnant flow field at the end of the cardiac cycle (Figure 4.1 J). Some residual stirring of the flow still remains at the end of the cycle and causes a small cycle-to-cycle variation in the measurements.

### **Flow field in a non-symmetric AAA**

a. Measurements in the symmetric plane. The flow field was measured in the symmetric plane (plane BB in Figure 2.3 (b)) in the partially ( $\beta = 0.5$ ) and fully ( $\beta = 1$ ) non-symmetric models, using the PIV system. The phase-averaged velocity, vorticity and stress fields are respectively shown in Figures 4.4 and 4.5 at times B to F.

During the accelerating phase of the systole, no appreciable qualitative difference can be observed between the flow in the non-symmetric and symmetric models: the flow stays attached to the walls, since the controlling parameter, the aspect ratio, is identical for all the models (Figures 4.4 B and 4.5 B). The effect of the non-symmetry becomes apparent, as the flow decelerates. Although a start-up vortex still forms when  $\beta = 0.5$  (model 17) followed by an internal shear layer (Figure 4.4 C), its progression is impaired by the three-dimensional patterns of the flow at times D and E. Even though the vortex ring is too weak to impinge on the distal wall, as would occur in the symmetric case, it persists through the diastole, before being dissipated in the resting period of the cardiac

cycle. The Stokes layer is therefore dominated by low vorticity and shear stresses throughout the diastole (Figure 4.4 D-E).

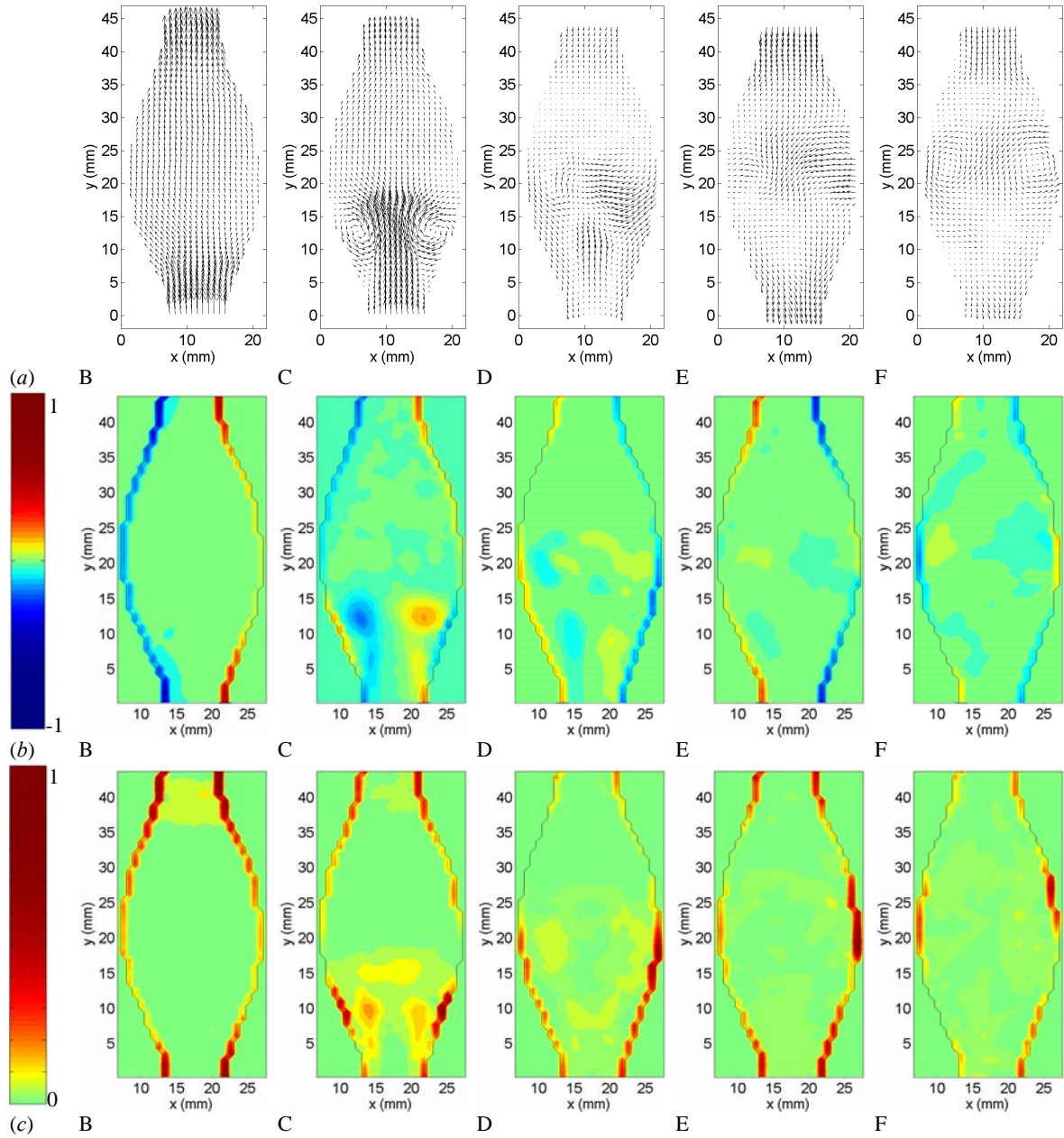


Figure 4.4: Non-dimensionalized phase-averaged velocity (a), vorticity (b) and stress (c) fields measured in the symmetric plane in model 17 ( $\beta = 0.5$ ) with the PIV system.

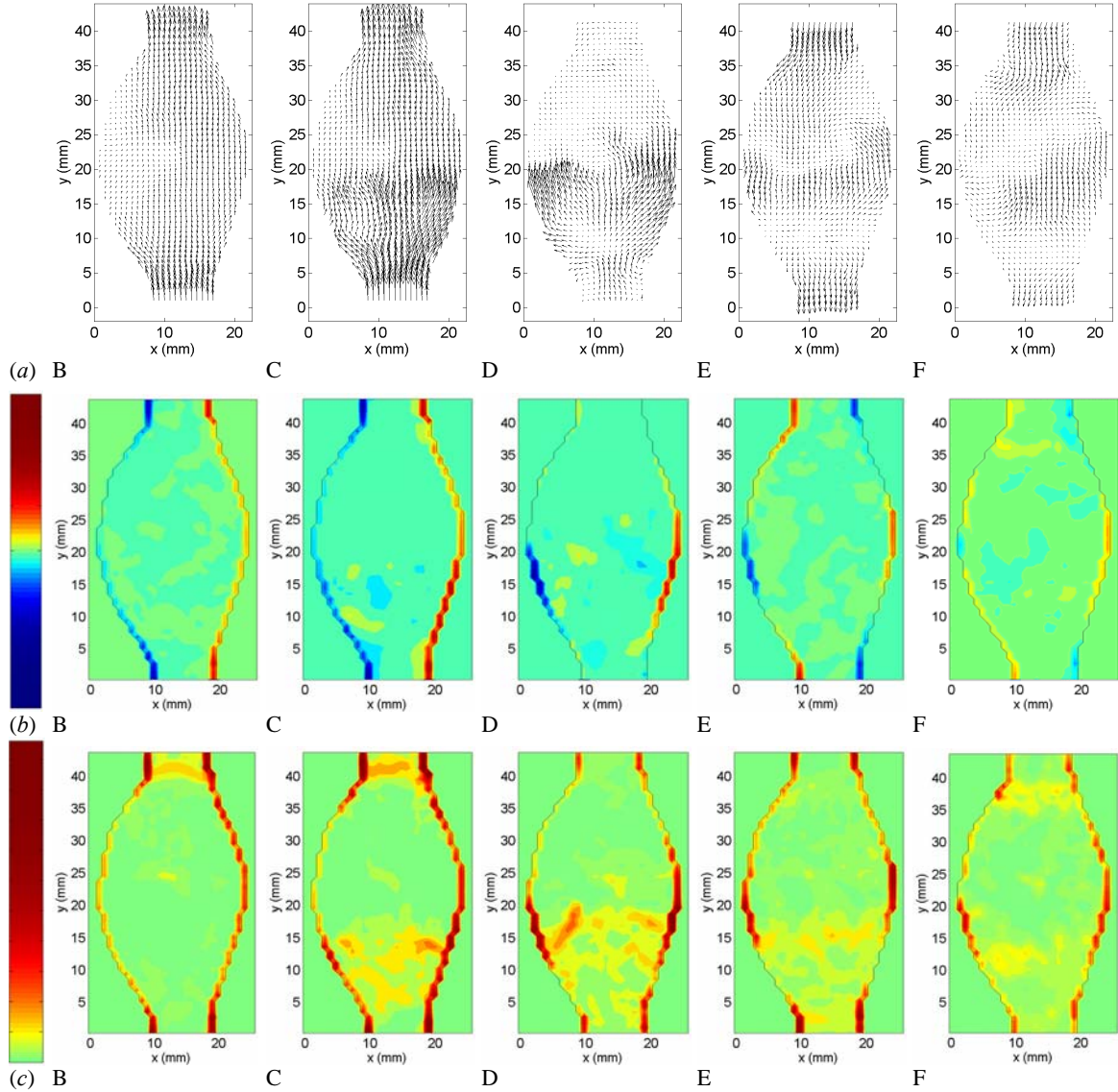


Figure 4.5: Non-dimensionalized phase-averaged velocity (*a*), vorticity (*b*) and stress (*c*) fields measured in the symmetric plane in model 18 ( $\beta = 1$ ) with the PIV system.

On the contrary, none of the flow features encountered in symmetric aneurysms (formation of a large start-up vortex ring and of internal shear layers, impingement of the vortex ring on the distal neck, breakdown of the axisymmetry in the diastole, etc.) are seen for large asymmetry parameters, as shown in Figure 4.5 for  $\beta = 1$  (model 18). We can see that, as the asymmetry parameter  $\beta$  increases to large values, the flow features are dominated by the very massive detachment that occurs in the non-symmetric plane.

b. Measurements in the non-symmetric plane. The instantaneous flow field measured in the non-symmetric mid-plane (plane CC on Figure 2.3 (b)) is shown in Figure 4.6 for  $\beta = 0.5$  (model 17) and in Figure 4.7 for  $\beta = 1$  (model 18) at times B to F, along with the vorticity and stress fields. One can notice that, for  $\beta = 1$ , the flow is no longer attached to the anterior wall during the systolic acceleration (Figure 4.7 B), when the flow is still attached for  $\beta = 0.5$  (Figure 4.6 B). For the flow waveform used in this experiment, the limiting dilatation ratio that guarantees no flow separation during the acceleration therefore lies between 3.1 and 4.5, which are, respectively, the equivalent dilatation ratios of the anterior wall in non-symmetric models 17 ( $\beta = 0.5$ ) and 18 ( $\beta = 1$ ).

The effect of the non-symmetry of the models is even more pronounced from the peak systole (time C) onwards, as the flow massively detaches: in the non-symmetric plane, the roll-up of the boundary layer into a strong vortex occurs only from the anterior proximal neck, while the flow remains attached to the posterior wall (see time C on Figure 4.6 for  $\beta = 0.5$  and time B on Figure 4.7 for  $\beta = 1$ ). This leads to the formation of a hairpin vortex. Flow separation occurs sooner as the asymmetry parameter increases. A small phase lag can be observed between the three sets of experiments. The points A, B, C, etc. are indicative of the time position in the cycle but due to the framing rate of our measurements, they do not correspond to exact times along the cardiac cycle.

After being formed, the hairpin vortex moves towards the posterior wall, inducing very high shear stresses at the location where it hits the wall (time D on Figure 4.6 for  $\beta = 0.5$  and time C on Figure 4.7 for  $\beta = 1$ ). The flow is seen to separate briefly from the wall downstream of the point of impact (Figure 4.7 C). For both models, it can be noted that the vortex is sufficiently strong to persist throughout the cardiac cycle. It is only washed out of the aneurysmal cavity at the systolic acceleration of the following cycle. It is this vortex that dominates the flow features in the case of  $\beta = 1$ , accounting for the disrupted flow patterns in the symmetric plane.

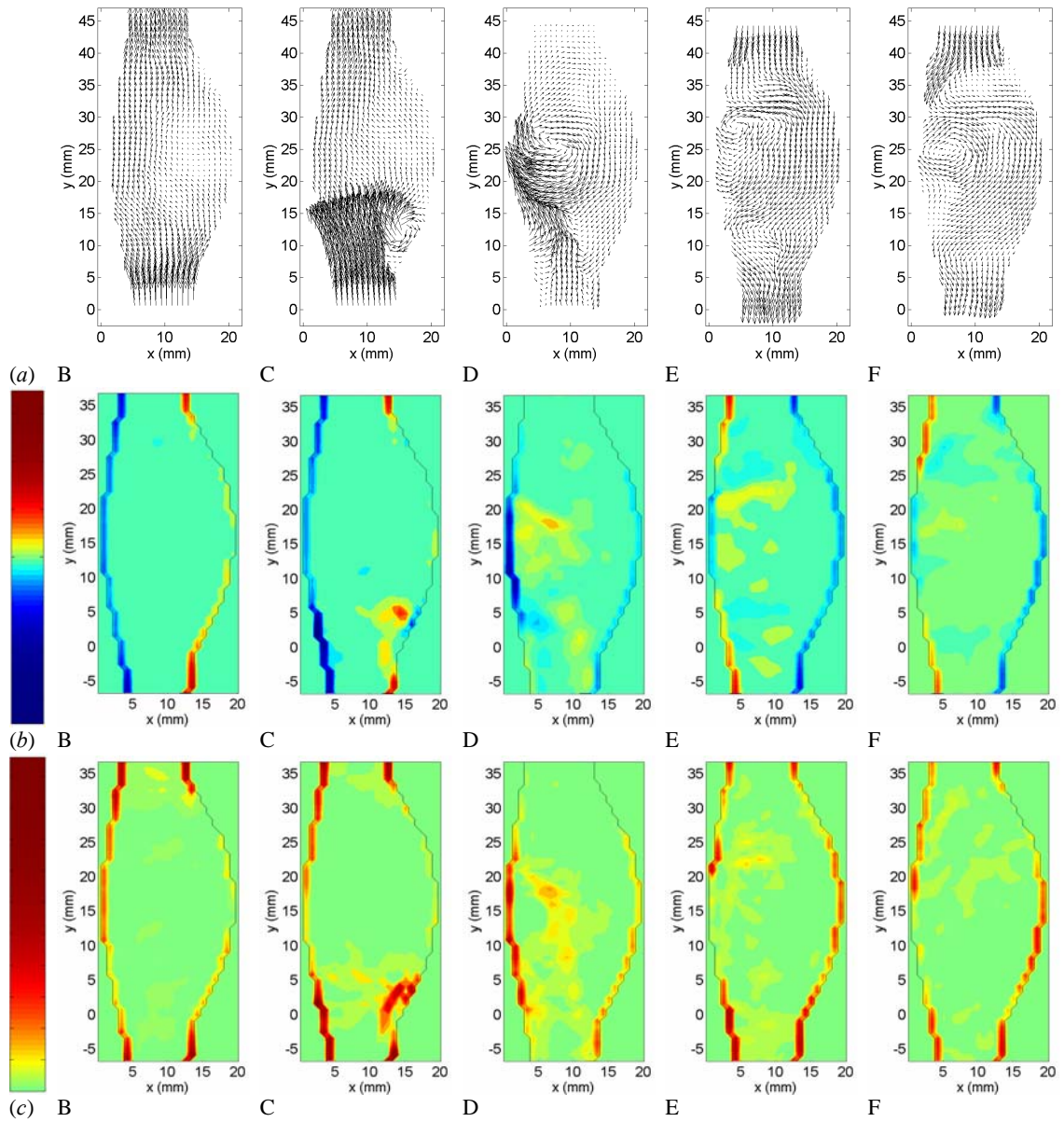


Figure 4.6: Non-dimensionalized instantaneous velocity (a), vorticity (b) and stress (c) fields measured in the non-symmetric plane in model 17 ( $\beta = 0.5$ ) with the PIV system.

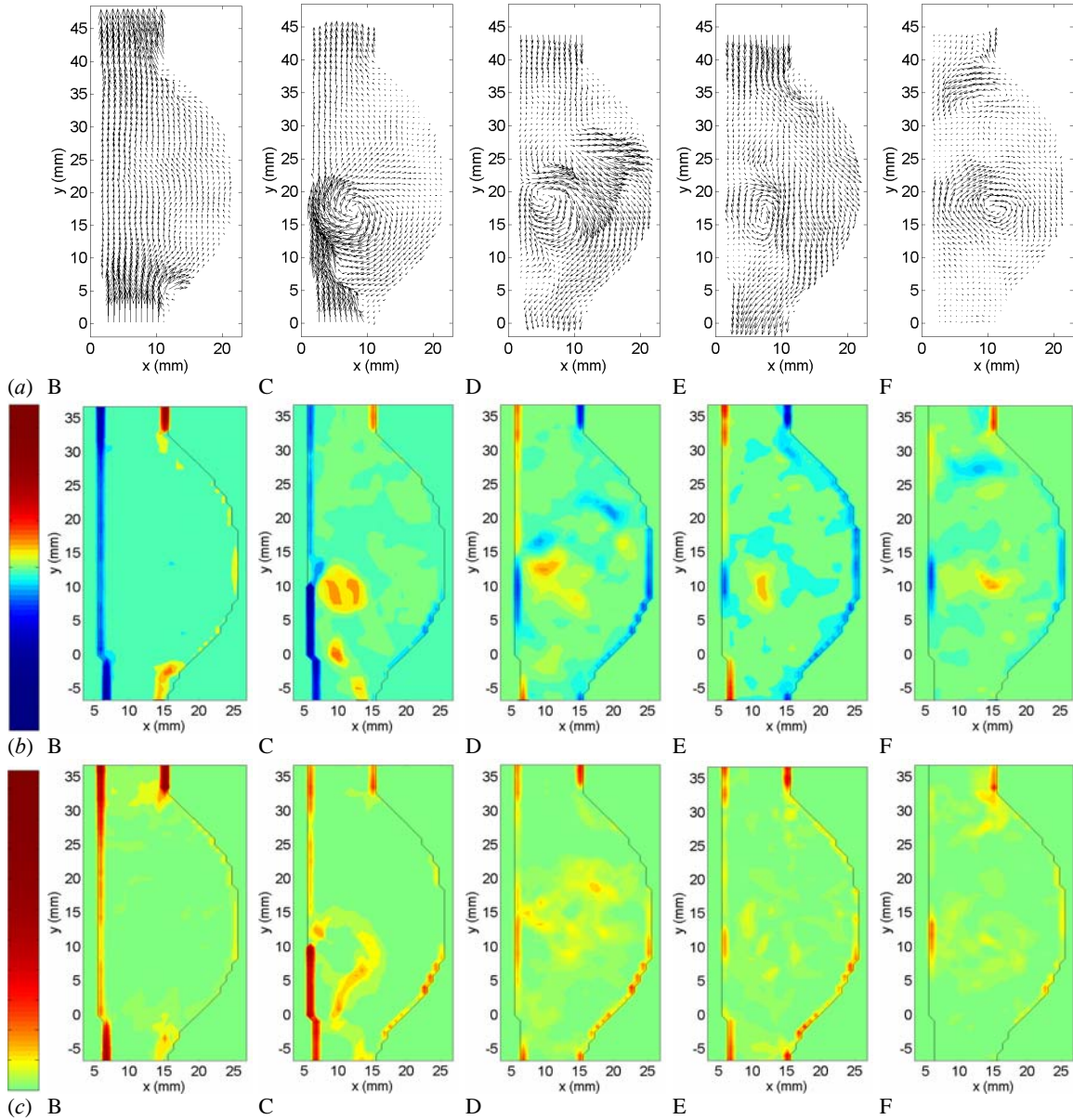


Figure 4.7: Non-dimensionalized instantaneous velocity (a), vorticity (b) and stress (c) fields measured in the non-symmetric plane in model 18 ( $\beta = 1$ ) with the PIV system.

One very important difference of the flow in non-symmetric geometries as compared to the symmetric case is the formation of a stagnation point along the bulged wall, as the detached flow impinges on the anterior wall. Our measurements show that this feature is enhanced as the asymmetry parameter is increased. The formation of a stagnation point is

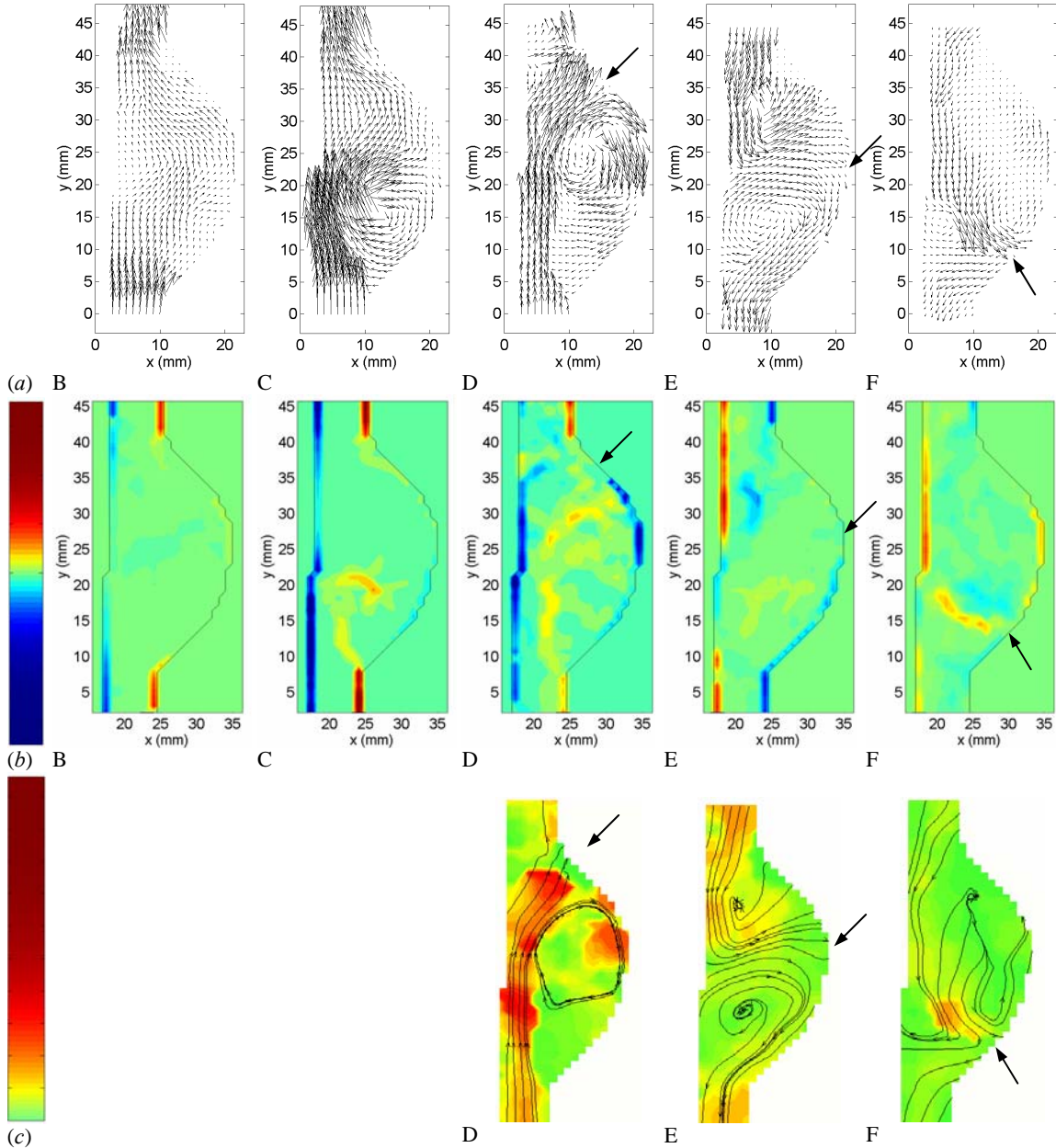


Figure 4.8: (a) Instantaneous velocity field measured in model 18 ( $\beta = 1$ ) with the same flow waveform but increased flow conditions ( $\overline{Re}_m = 540$ ,  $\overline{Re}_p = 4550$ ), (b) corresponding non-dimensionalized instantaneous vorticity field, (c) streamlines superimposed on the plot of the non-dimensionalized instantaneous velocity magnitude. The arrow indicated the location of the stagnation point.

only incipient for  $\beta = 0.5$  (Figure 4.6 F), but it is more pronounced for  $\beta = 1$  (Figure 4.7 D and E). The stagnation point, characterized by a large spike in pressure and spatial

gradients of wall shear stress appears towards the point of maximum diameter, damaging the wall at what seems to be its weakest point. Increasing the Reynolds number strengthens the stagnation point. At high Reynolds numbers, the stagnation point is observed to form distally and then sweep the entire anterior wall (Figure 4.8).

## 2. Patterns of WSS and GWSS in AAAs

### WSS in a symmetric AAA

Detailed results of the spatial and temporal distribution of WSS in different symmetric aneurysms has already been described (Chapter 3). In order to ascertain the effects of the loss of symmetry on the WSS, we briefly discuss here the most relevant features. With respect to the WSS and GWSS, the two dramatic events in the case of a symmetric aneurysm, are the formation of a start-up vortex ring and its later impingement on the distal neck.

The phase-averaged WSS, measured in the symmetric model (model 16) and non-dimensionalized by the peak WSS of the healthy vessel, are shown in Figure 4.9 (a). The corresponding gradients of the phase-averaged WSS are given in Figure 4.9 (b). The convention followed is to assign a negative value to the WSS in regions of reversed flow. During the systolic acceleration ( $t/T = 0.2$ ), the WSS are much smaller along the aneurysm wall than in the parent vessel. Since the flow stays attached to the walls at this stage, the WSS evolve similarly to the velocity, which inversely scales with the diameter in order to conserve mass. The subsequent large decrease in WSS that occurs at the aneurysm necks induces very strong gradients of WSS at these locations ( $y/d = 0$  and  $4.6$  at times  $t/T = 0.2$  and  $0.3$ ). Some level of GWSS persists at the necks throughout the cardiac cycle. The flow detachment from the wall at  $t/T = 0.3$  gives rise to a region of large negative WSS around  $y/d = 0.6-0.8$ . The formation of the strong vortex ring also leads to the generation of very large GWSS upstream and downstream of it. The impact

of the vortex ring on the distal wall at  $t/T = 0.5$  is associated with the formation of very large negative WSS at  $y/d = 3.6$  and high GWSS around this point.

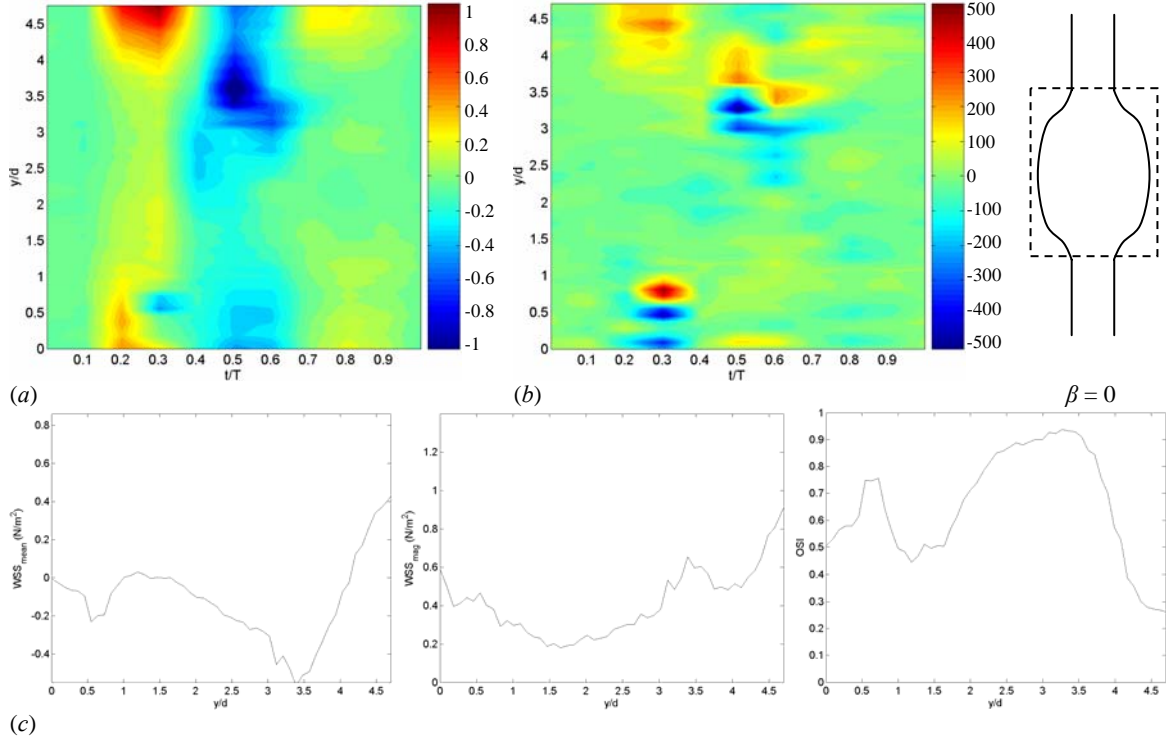


Figure 4.9: (a) Phase-averaged WSS measured in the symmetric model (model 16), non-dimensionalized by the peak WSS of the healthy vessel. (b) Gradient of the phase-averaged WSS in  $N/m^3$ . (c) Mean WSS, magnitude of the WSS and oscillating shear index.

The evolution of the time-averaged WSS,  $WSS_{mean}$ , magnitude of the WSS,  $WSS_{mag}$ , and of the oscillatory shear index,  $OSI$  (see definitions in the previous chapter), is shown in Figure 4.9 (c). The formation of an AAA has a very important effect on all these parameters. In the symmetric case, the  $WSS_{mean}$  drops from  $0.35 N/m^2$  in a healthy abdominal aorta to an average of  $-0.11 N/m^2$  in the aneurysm, the  $WSS_{mag}$  decreases from  $1.2-1.3 N/m^2$  to an average of  $0.42 N/m^2$  and the  $OSI$  index increases from  $0.3$  to an average of  $0.65$ . In conclusion, the aneurysm walls are subjected to WSS of low magnitude and the flow inside the AAA is mainly reversed, as indicated by the  $WSS_{mean}$  and the  $OSI$  index.

More specifically, the flow separation from the wall leads to a region, where the WSS are very low and oscillating ( $OSI \sim 0.5$ ) through most of the cardiac cycle ( $y/d = 0.7-2$ ). The distal half of the aneurysm is dominated by the presence of the vortex ring, which induces reversed flow conditions, as indicated by the OSI index being well above 0.5. The peak ( $OSI = 0.93$ ) occurs at the location of the vortex ring impingement on the wall, where the  $WSS_{mean}$  drops to very high negative values ( $-0.55 \text{ N/m}^2$ ). The distal half is also subjected to sustained gradients of WSS.

### **WSS in a non-symmetric AAA**

a. Measurements in the symmetric plane. The measurements of the phase-averaged WSS and GWSS, along with the evolution of the  $WSS_{mean}$ ,  $WSS_{mag}$  and  $OSI$  index, are shown in Figures 4.10 and 4.11, taken in the symmetric plane of models 17 ( $\beta = 0.5$ ) and 18 ( $\beta = 1$ ), respectively. As discussed in the previous section, the flow in the symmetric plane of model 17 retains most of the characteristics seen in an axisymmetric model. The WSS patterns are likewise characterized by a marked decrease during systole, which leads to GWSS at the necks. The magnitude of the stimulation on the wall is very comparable, with an average  $WSS_{mag}$  of  $0.40 \text{ N/m}^2$ . The formation of the large vortex induces a zone of negative WSS and higher GWSS around it, although the intensity of the GWSS is three times lower than in the axisymmetric model. The main difference with the symmetric model comes from the trajectory of the vortex. For  $\beta = 0.5$ , the vortex stays confined to the proximal half and does not impinge on the distal wall. Since it is not disturbed by the vortex, the distal half of the AAA is dominated by a  $WSS_{mean}$  very close to the healthy value ( $\sim 0.3 \text{ N/m}^2$ ). Contrary to the symmetric model, the  $WSS_{mean}$  is then on average positive inside the aneurysm ( $\overline{WSS_{mean}} = 0.13 \text{ N/m}^2$ ) and the average  $OSI$  index remains in the healthy range ( $\overline{OSI} = 0.36$ ).

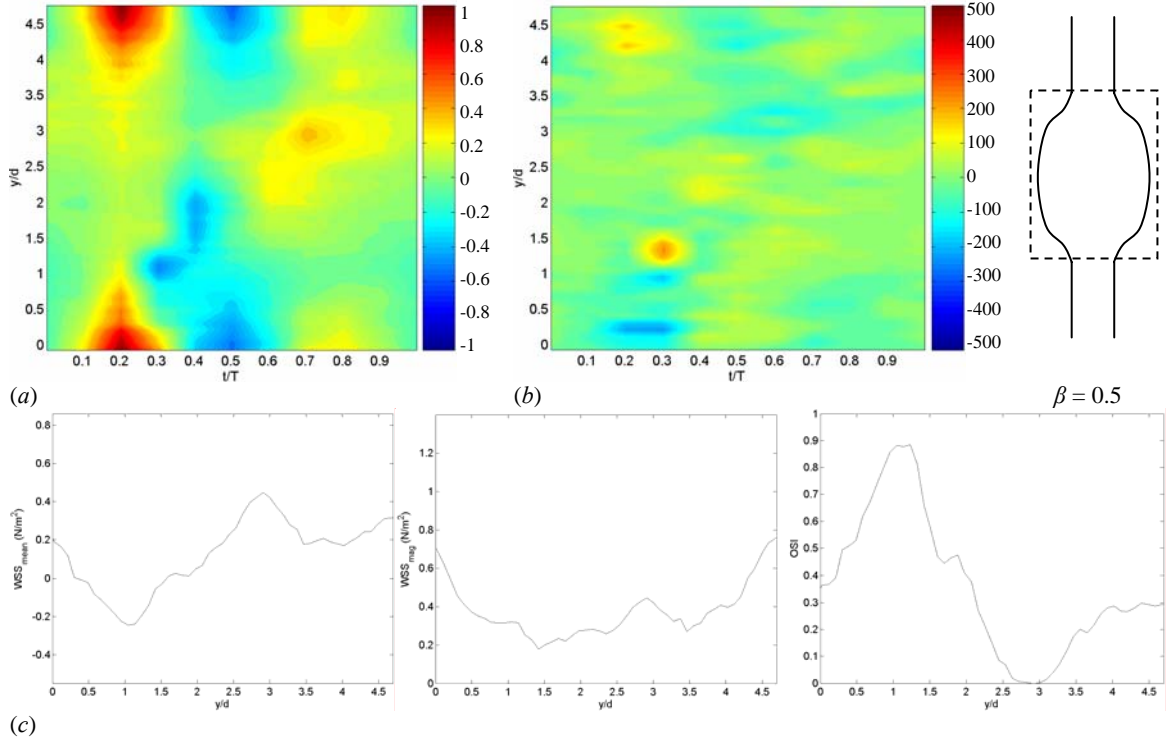


Figure 4.10: (a) Phase-averaged WSS measured in the symmetric plane in model 17 ( $\beta = 0.5$ ), non-dimensionalized by the peak WSS of the healthy vessel. (b) Gradient of the phase-averaged WSS in  $\text{N/m}^3$ . (c) Mean WSS, magnitude of the WSS and oscillating shear index.

In the case of  $\beta = 1$ , however, the proximal walls are subjected to positive WSS in the decelerating portion of the systole, with values close to the ones measured in a healthy vessel. This explains why the  $WSS_{mean}$  does not decrease sharply in the proximal half and remains around  $0.2 \text{ N/m}^2$ . The distal half is dominated by negative WSS of very small magnitude ( $WSS_{mag} \sim 0.2 \text{ N/m}^2$ ), situation that corresponds to a high value of the  $OSI$  index ( $\sim 0.8$ ). GWSS form at the transition between the 2 regions of the AAA in the late systole ( $y/d = 2.2$  at  $t/T = 0.4$ ).

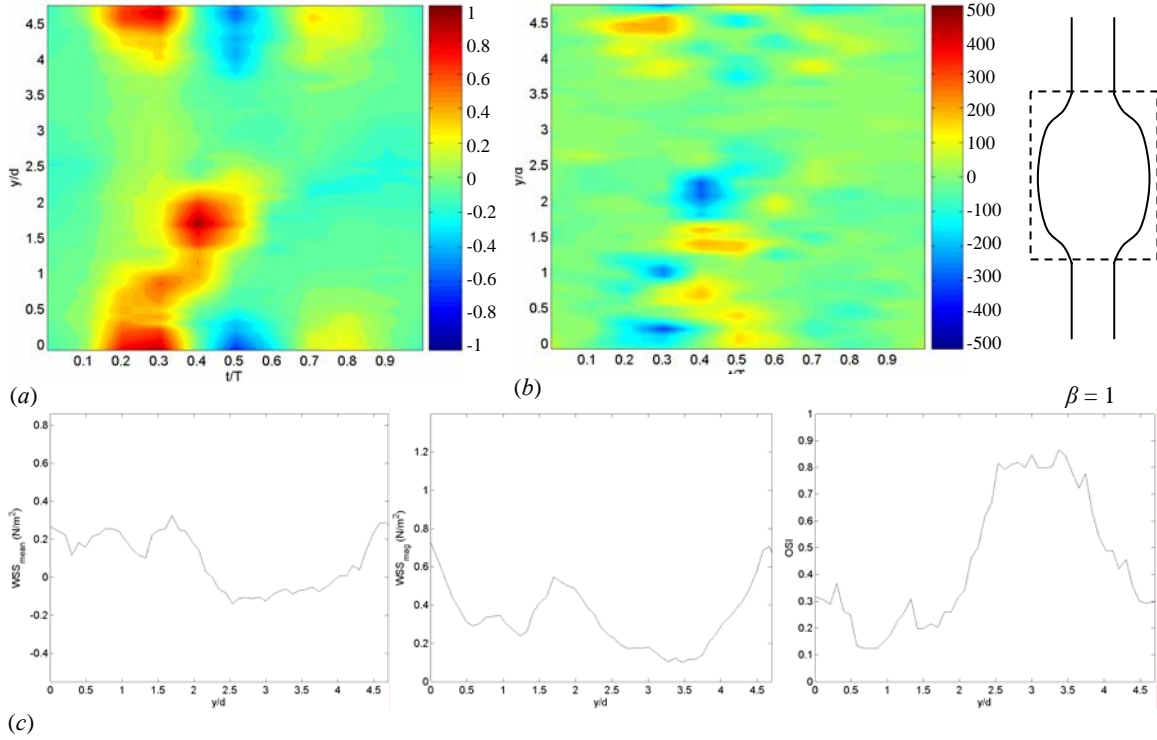


Figure 4.11: (a) Phase-averaged WSS measured in the symmetric plane in model 18 ( $\beta = 1$ ), non-dimensionalized by the peak WSS of the healthy vessel. (b) Gradient of the phase-averaged WSS in  $N/m^3$ . (c) Mean WSS, magnitude of the WSS and oscillating shear index.

b. Measurements in the non-symmetric plane. The WSS and GWSS measured in the non-symmetric plane of models 17 ( $\beta = 0.5$ ) and 18 ( $\beta = 1$ ) are shown in Figures 4.12 and 4.13 for the posterior wall and in Figures 4.14 and 4.15 for the anterior wall.

The peculiarity along the posterior wall is the persistence of a mean forward flow in the non-symmetric models. With high WSS acting on the proximal half of the AAA ( $\sim 0.46 N/m^2$  on average), the  $OSI$  index even drops to a zero value (forward flow) in the middle portion of the wall. The average  $OSI$  index is consequently much lower along the posterior wall than in the healthy vessel ( $\overline{OSI} = 0.20$ ), when the average  $WSS_{mean}$  is of the same order of magnitude ( $\overline{WSS}_{mean} = 0.37 N/m^2$ ). The average  $WSS_{mag}$  is higher as well than anywhere else in the aneurysm, but at  $0.58 N/m^2$ , it remains still far from the healthy value. A positive peak in WSS occurs at the location, where the vortex, formed at

the anterior proximal neck touches the posterior wall. At this location (at  $y/d = 2.5$  and  $t/T = 0.4$  for  $\beta = 0.5$  and  $y/d = 1.8$  and  $t/T = 0.3$  for  $\beta = 1$ ), the vortex induces a very high value of  $WSS_{mean}$  and  $WSS_{mag}$  as well as high gradients of WSS. Downstream of the point of impact, the WSS progressively match with the healthy vessel values.

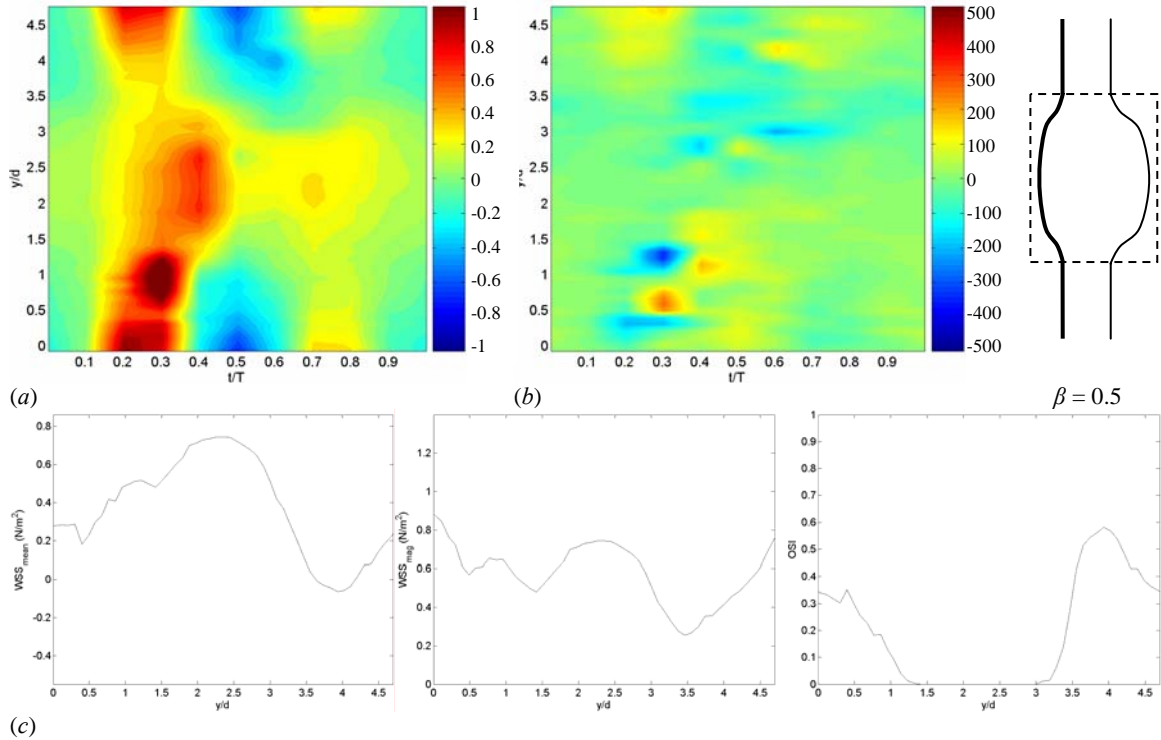


Figure 4.12: (a) Phase-averaged WSS measured in the non-symmetric plane in model 17 ( $\beta = 0.5$ ) along the posterior wall, non-dimensionalized by the peak WSS of the healthy vessel. (b) Gradient of the phase-averaged WSS in N/m<sup>3</sup>. (c) Mean WSS, magnitude of the WSS and oscillating shear index.

While the posterior wall is mainly stimulated by positive WSS, the anterior wall is dominated by an almost fully reversed flow with very low WSS throughout the cardiac cycle. The particularity of the anterior wall is the presence of a very large region of slowly recirculating flow that extends over most of the wall. This region, characterized by an *OSI* index of 1 (fully reversed flow) is dominated by negative WSS of very low magnitude ( $\overline{WSS}_{mean} = -0.20$  N/m<sup>2</sup>,  $\overline{WSS}_{mag} = 0.20$  N/m<sup>2</sup>). The very marked decrease in the WSS at the necks generates strong gradients of WSS, twice as large as the ones

measured in the axisymmetric model. Note that the proximal neck is not resolved on the measurements in model 18 ( $\beta = 1$ ).

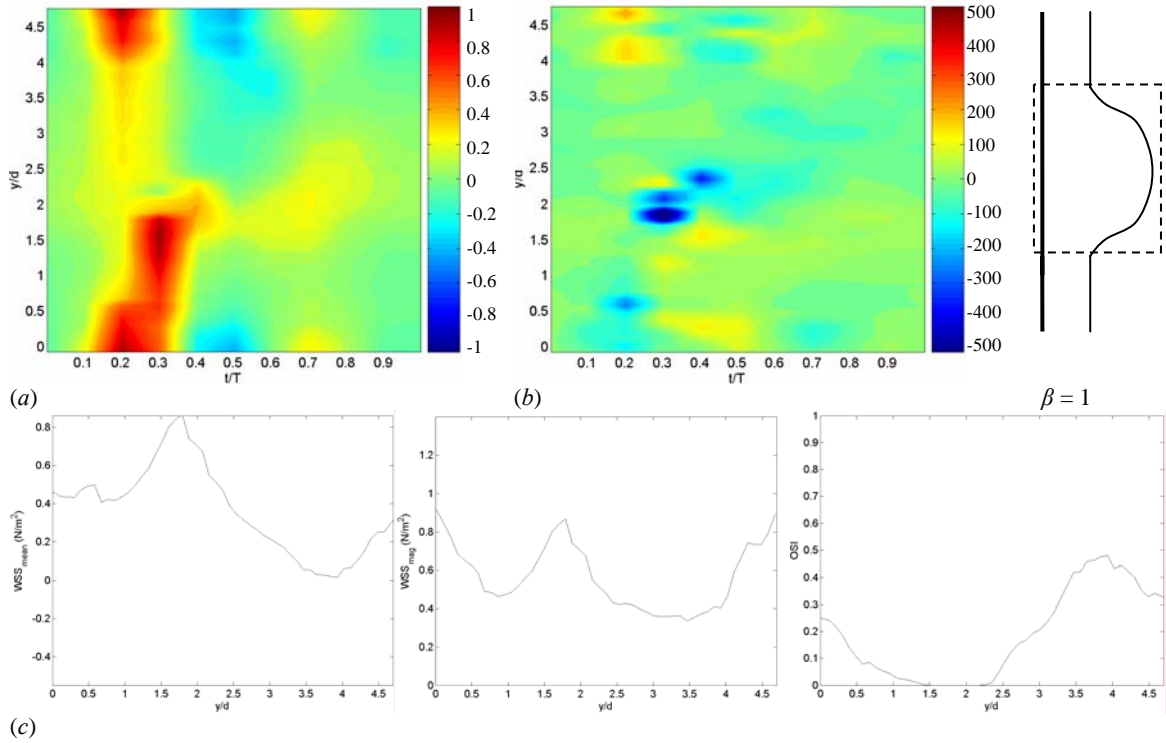
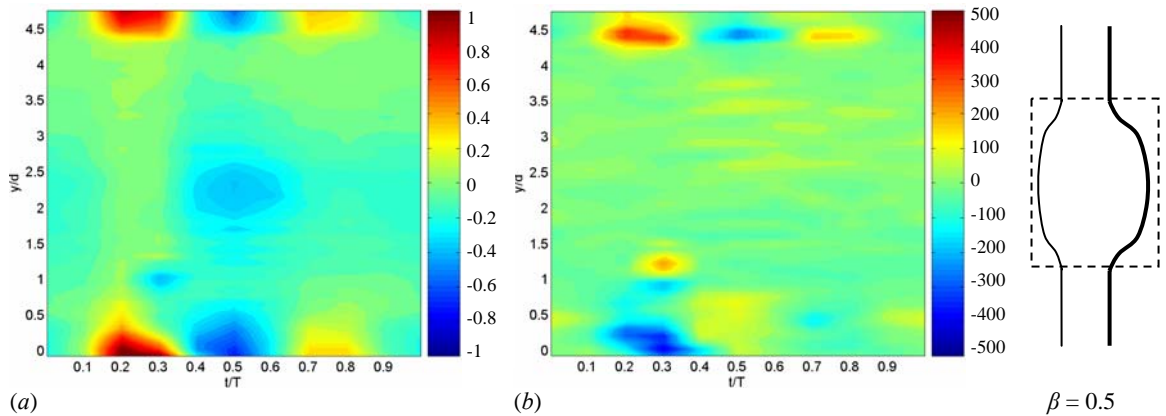
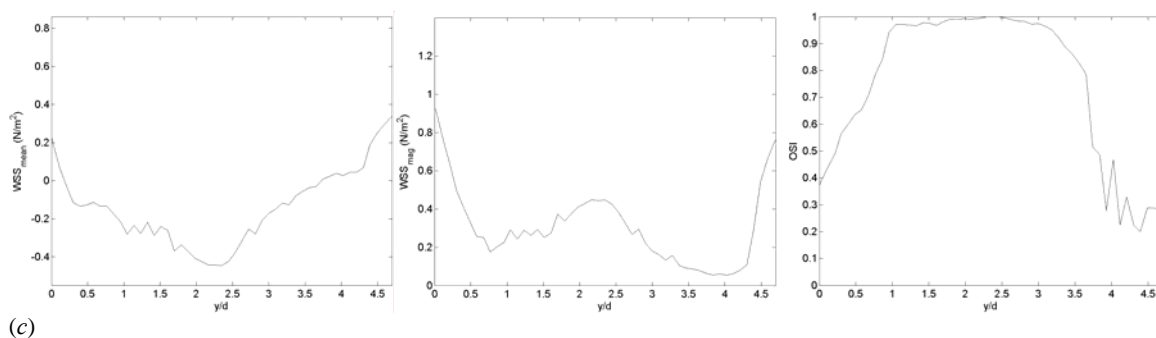


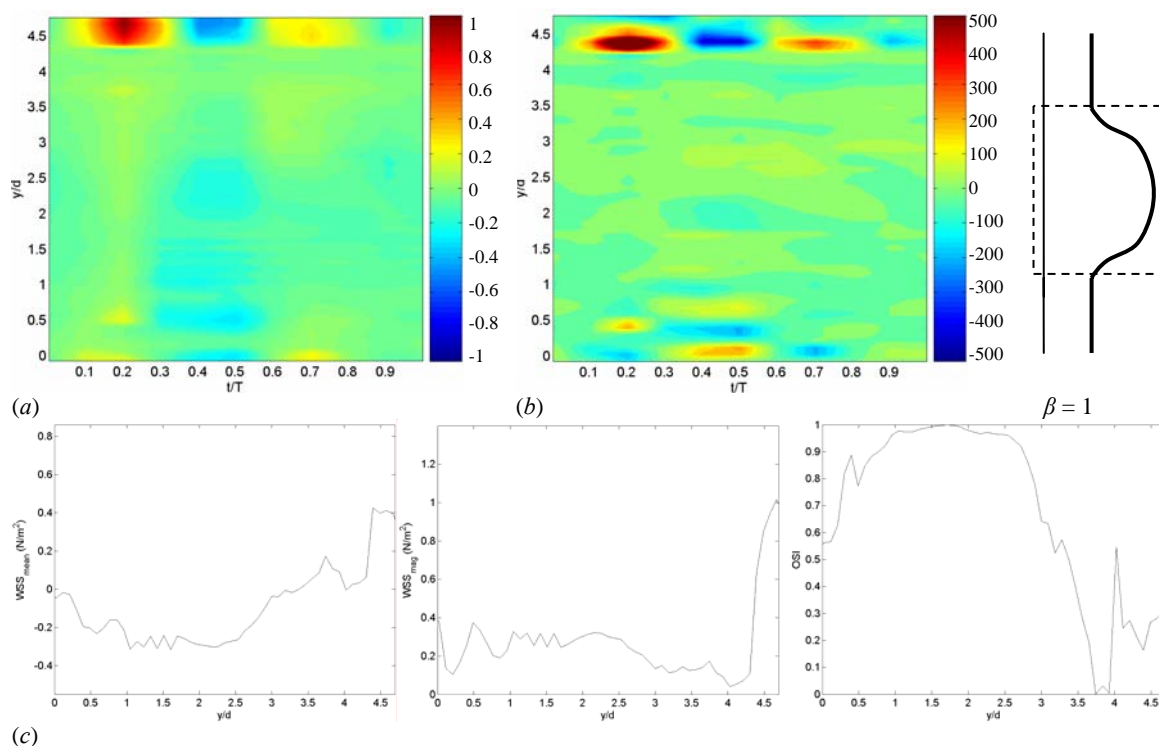
Figure 4.13: (a) Phase-averaged WSS measured in the non-symmetric plane in model 18 ( $\beta = 1$ ) along the posterior wall, non-dimensionalized by the peak WSS of the healthy vessel. (b) Gradient of the phase-averaged WSS in  $N/m^3$ . (c) Mean WSS, magnitude of the WSS and oscillating shear index.





(c)

Figure 4.14: (a) Phase-averaged WSS measured in the non-symmetric plane in model 17 ( $\beta = 0.5$ ) along the anterior wall, non-dimensionalized by the peak WSS of the healthy vessel. (b) Gradient of the phase-averaged WSS in  $\text{N/m}^3$ . (c) Mean WSS, magnitude of the WSS and oscillating shear index.



(c)

Figure 4.15: (a) Phase-averaged WSS measured in the non-symmetric plane in model 18 ( $\beta = 1$ ) along the anterior wall, non-dimensionalized by the peak WSS of the healthy vessel. (b) Gradient of the phase-averaged WSS in  $\text{N/m}^3$ . (c) Mean WSS, magnitude of the WSS and oscillating shear index.

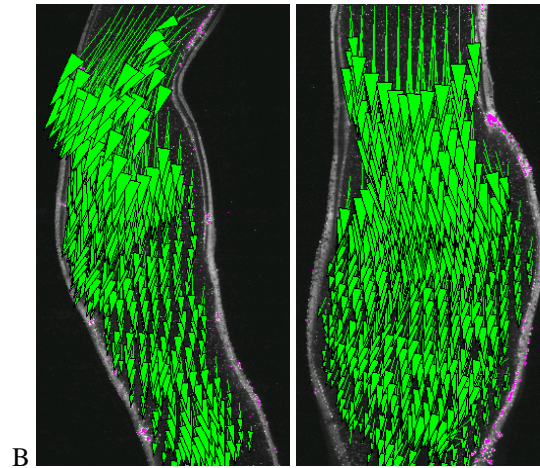


Figure 4.16: Phase-averaged velocity field measured in the left and posterior planes in the anatomically correct model at time B.

### 3. Extension to anatomically correct geometries

In order to relate these results measured in non-realistic models of AAA to anatomically correct aneurysms, we reconstructed a real shape aneurysm from CT scan images and tested it in vitro – see method in Appendix C. The present aneurysm is fusiform and it is large enough to have evolved into a non-symmetric shape ( $D/d = 2.7$ ,  $L/d = 5.7$ ). One can notice that this patient presents a larger curvature of the infrarenal aorta and a kink upstream of the aneurysm. PIV measurements of the velocity field were taken in two perpendicular planes. Figure 4.16 shows the velocity measured at time B in the left and posterior views. Similarly to what was observed in the experiments in the straight rigid models, the flow remains attached to the walls until the peak systole. In the decelerating portion of the cardiac cycle, the flow separates from the posterior and lateral walls (Figure 4.17 C). A large recirculating region is formed along the posterior wall downstream of the kink and along part of the lateral walls, subjecting them to low WSS. The anterior wall is simultaneously subjected to high WSS due to the large curvature of the vessel wall. Circumferential GWSS are therefore created, which may affect the

endothelial cells in the intermediate regions. The flow then reverses in the diastole, as shown in Figure 4.17 E. A transition to a weak turbulent state can be observed at that time.

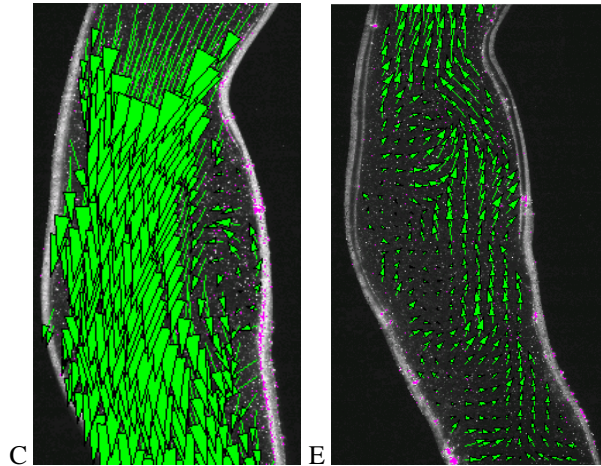


Figure 4.17: Phase-averaged velocity field measured in the left plane in the anatomically correct model at times C and E.

The measurements taken in the anatomically correct AAA model reinforce the likelihood of a correlation between architectural changes in the arterial trunk and the abdominal aortic aneurysm disease. In the case of the aneurysm reconstructed, the patient presents an increased bending of the infrarenal aorta and a kink below the bifurcation to the renal arteries. It is interesting to notice that the aneurysm has developed downstream of the kink. It is quite improbable that the aneurysm developed because of an increase in the static pressure, since it would have otherwise developed upstream of the constriction. It is more likely that the aneurysm developed due to the disturbed flow conditions induced by the abnormal anatomy.

## D. Discussion

We have measured the spatial and temporal distribution of the wall shear stresses in idealized models of AAAs of increasing asymmetry parameter. It has been shown that most of the flow characteristics found in symmetric aneurysms persist in non-symmetric models of AAA. Up to large asymmetry parameters, the flow remains likewise attached to the walls in the accelerating portion of the systole. This engenders a decrease in the WSS inside the aneurysm as compared to the healthy vessel and therefore large GWSS at both necks. In an experiment conducted in model 16 ( $D/d = 2.4$ ,  $L/d = 4.5$ ,  $\beta = 0$ ) with a sinusoidal flow waveform ( $\langle \overline{Re} \rangle = 1700$ ,  $\overline{Re}_p = 2200$ ), we have found that the flow does not reattach to the walls during systole, because of the too small systolic acceleration. Instead, a jet forms at the proximal neck in the early systole and discharges into the bulging cavity, preceded by a start-up vortex ring (Figure 4.18). An array of vortices forms in the shear layer, as the jet meanders through the aneurysm. In the case of large aspect ratios, such as in model 16, a helical instability may develop, as indicated by the staggered configuration of the counter-rotating vortices (Figure 4.18 (b)). This example shows the importance of reproducing adequately the flow waveform, the key events being the strong acceleration and deceleration generated *in vivo* in the systole.

In the case of the physiological flow waveform (Figure 2.5), a non-uniform separation occurs from the proximal neck as the flow decelerates. The geometric asymmetry affects flow separation and prevents the formation of a closed vortex ring as measured in axisymmetric models. Instead, a helical flow pattern develops in the AAA. The strongest vortex that is shed from the proximal anterior wall, where the wall curvature is maximal takes the shape of a hairpin vortex. As it progresses inside the aneurysm, it rotates in the cavity. The stretching of the vortex in the axial direction is much more important than in a symmetric aneurysm model. The strength of the vortex shed from the anterior wall also increases with the asymmetry parameter. In the case of

very large  $\beta$ , it is so strong that the hairpin vortex already impinges on the posterior wall in the early diastole. The increase in the vortex strength and stretching as  $\beta$  increases is likely to generate a stronger transition to turbulence in the diastole, although the turbulent intensity still remains weak.

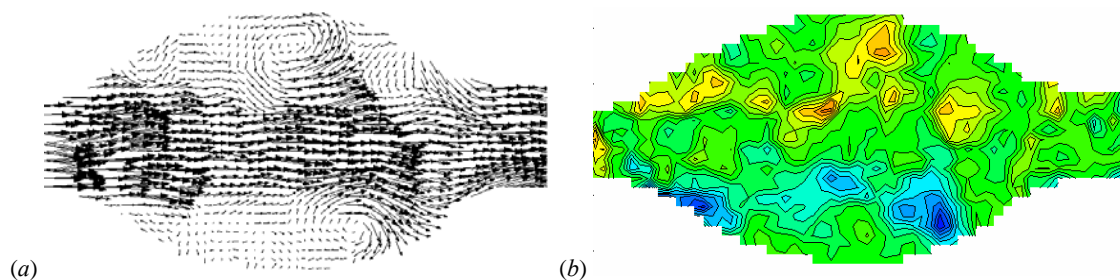


Figure 4.18: Instantaneous velocity (a) and vorticity fields (b) measured at peak systole in the symmetric model (model 16) under a sinusoidal flow waveform.

Associated with this vortex are opposite patterns of WSS for the posterior and anterior walls. Because of the formation of a large recirculation zone, the endothelial cells along the anterior wall are subjected to very low and reversed WSS. Averaged over the length of the aneurysm and one cardiac cycle, the magnitude of the WSS is less than 20% of the value in a healthy aorta. Such a low level of stimulation is likely to greatly impair the endothelium, as discussed in the introduction. At stake is also the unidirectional quasi-steady stress pattern (in this case negative WSS) (Figure 4.19 (a)). In a healthy vessel, the VEC are exposed to pulsatile WSS that become negative only during diastole. Steady low shear stresses have been extensively studied in the literature and have been reported to lead to an increase in the rate of cell proliferation and apoptosis. In regions of quasi-stasis, the residence times increase drastically, enhancing all the diffusion processes through the walls. The flow conditions found along the anterior wall are therefore likely to promote the local accumulation of molecules such as low-density lipoproteins in the intima and media layers, leading to an inflammation of the vessel wall (Caro, Fitz-Gerald & Schroter 1971). Platelets and debris are also likely to deposit along

the wall. We can thus hypothesize that an endoluminal thrombus may form in these large regions of slowly recirculating flows.

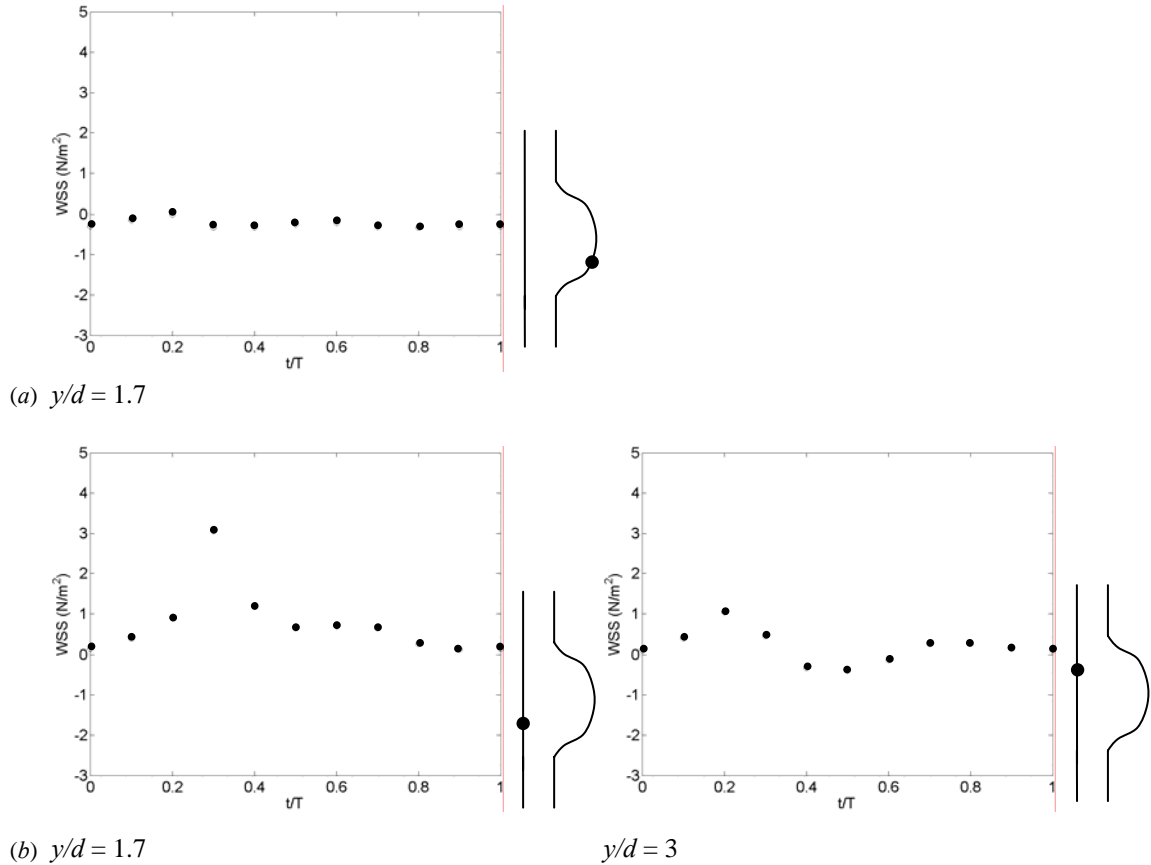


Figure 4.19: Phase-averaged profiles of WSS measured in model 18 ( $\beta = 1$ ) at  $y/d = 1.7$  along the anterior wall (a) and at  $y/d = 1.7$  and 3 along the posterior wall (b).

On the opposite wall, the endothelial cells of the proximal half are subjected to only positive WSS (forward flow) of much higher amplitude (Figure 4.19 (b)). Still the average magnitude is lower than in a healthy vessel ( $\sim 60\%$ ), because of the influence of the bulging. A peak in WSS occurs in the region, where the vortex impinges the wall around  $y/d = 1.5-1.7$ . The distal half of the posterior wall, however, experiences oscillating WSS of about  $1 \text{ N/m}^2$ -amplitude (Figure 4.19 (b)). The difference in WSS patterns along the posterior wall generates GWSS in the medial section. Furthermore,

with the posterior and anterior walls subjected to radically opposite patterns of WSS, strong circumferential gradients of WSS are likely to be generated along the lateral walls.

## **E. Conclusion**

We have quantified the effects of the loss of symmetry on the spatial and temporal distribution of wall shear stresses in abdominal aortic aneurysms. The measurements conducted in rigid non-symmetric models of AAA have indicated that some of the typical flow features measured in symmetric models persist. The flow remains attached during the systolic acceleration, although a limiting dilatation ratio exists above which the acceleration is not sufficient to guarantee it. Similarly to symmetric models, it has been observed that flow separation from the proximal neck occurs earlier when the dilatation ratio increases, which corresponds in this study to an increase in the asymmetry parameter  $\beta$ . However, the geometrical asymmetry leads to a situation, where the flow remains attached to the posterior wall, which prevents the shedding of a closed vortex ring. The largest vortex is shed from the anterior wall, where the local dilatation ratio is the highest. Its strength increases with the asymmetry parameter.

The massive detachment from the anterior wall and the shedding of this prominent vortex dictate the major changes in the WSS patterns. On the one hand, the anterior wall is subjected to very low shear stresses ( $\overline{WSS}_{mean} = -0.20 \text{ N/m}^2$ ) that are not only fully reversed ( $OSI = 1$ ) but also quasi-steady. Associated with this very slowly recirculating flow are long resident times that will promote the formation of an endoluminal thrombus. While the endothelial cells experience practically no shear stresses, the proximal and distal necks are weakened by very strong gradients of WSS.

On the other end, the proximal half of the posterior wall, up to the point of impact of the vortex, is subjected to forward flow ( $OSI = 0$ ), with higher magnitude wall shear stresses. Without the influence of the vortex, the peak WSS naturally decreases in the

distal half generating high gradients of WSS downstream of the impact point. High gradients are also expected in the longitudinal direction along the lateral wall, since the anterior and posterior walls experience WSS in two opposite directions.